Cellulose (2019) 26:2639–2651
https://doi.org/10.1007/s10570-019-02247-w

ORIGINAL RESEARCH

Printing and mechanical characterization of cellulose nanofibril materials

Lisa M. Mariani · William R. Johnson III · John M. Considine · Kevin T. Turner

Received: 5 July 2018 / Accepted: 2 January 2019 / Published online: 11 January 2019

Abstract Cellulose nanofibrils (CNF) are a promising building block of structural materials because they are biodegradable, can be made into optically transparent bulk materials, and have exceptional specific strength and stiffness compared to common synthetic polymers. The manufacturing of bulk materials from CNFs is a challenge because CNFs form networks in solution at low solids concentration, which can result in long processing times as well as large residual stresses and distortion upon water removal. Here, a method to form materials from CNF suspensions via direct ink writing, a type of additive manufacturing, is demonstrated. Multilayer printing of CNFs provides a route to control drying time by depositing thin layers one at a time. A printing system with a pressure-controlled dispensing system was used to deposit aqueous CNF suspensions onto a temperature-controlled substrate. The geometry, roughness, and mechanical properties of the printed structures were characterized. The shape of the printed line profile is controlled by a combination of the wettability of the substrate, dispense rate, printing speed, and temperature of the substrate. Spatial variation of the elastic modulus of printed CNF structures was assessed with nanoindentation and the average percent difference was found to be small at ± 2.6% of the mean over the area of the printed lines. Through multilayer printing freestanding films with thicknesses greater than 60 μm were achieved. Tensile specimens were printed and characterized; a tensile strength of 72.6 MPa ± 7.4 MPa and a Young's modulus of 10.2 GPa ± 1.2 GPa were measured.

L. M. Mariani · W. R. Johnson III · K. T. Turner (✉)
Department of Mechanical Engineering and Applied Mechanics, University of Pennsylvania, Philadelphia, PA 19104, USA
e-mail: kturner@seasu.upenn.edu

J. M. Considine
USDA Forest Service, Forest Products Laboratory, Madison, WI 53726, USA

Graphical abstract

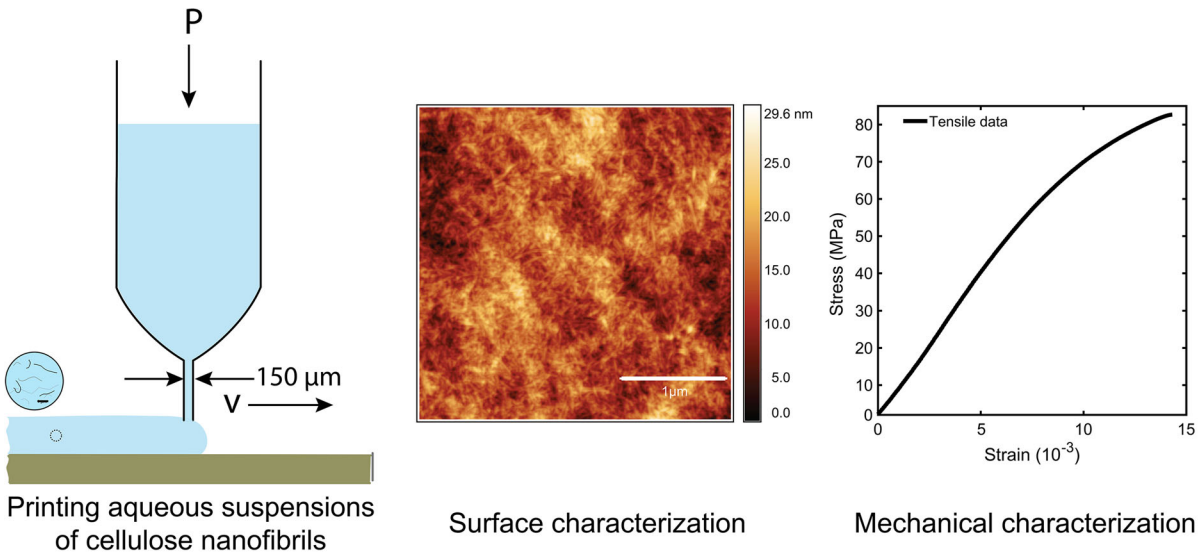

Keywords Nanocellulose · Cellulose nanofibers · Nanofibrillated cellulose · Printing · Additive manufacturing · Mechanical properties

Introduction

Cellulose nanofibrils (CNFs) are biodegradable, often optically transparent when formed into bulk materials, have diameters of approximately 10 nm, aspect ratios > 100, and have high specific strength and specific stiffness (Isogai 2013; Baez et al. 2014). CNFs have multiple applications, including as a reinforcing phase in composites, coatings for paper and packaging, substrates for flexible electronics, and filtration components (Isogai 2013; Shatkin et al. 2014; Carpenter et al. 2015). Neat solid CNF materials have traditionally been prepared in the form of sheets by removing water from an aqueous CNF solution via techniques such as room temperature drying, oven drying, vacuum filtration, and pressure filtration. CNF films made via these techniques can have tensile strengths greater than 200 MPa and Young's moduli greater than 11 GPa (Henriksson et al. 2008; Fukuzumi et al. 2009; Aulin et al. 2012; Malho et al. 2012; Sehaqui et al. 2012; Wu et al. 2012; Zhu et al. 2015). Furthermore, several studies have shown the stiffness of CNF sheets can be increased further by aligning the CNFs through drawing or constrained drying processes (Sehaqui et al. 2012; Baez et al. 2014).

Additive manufacturing, also referred to as 3D printing, is an approach that can be used to print a wide range of materials, including polymers, ceramics, and metals (Berman 2012; Gross et al. 2014). In a specific type of 3D printing known as direct ink writing, shear thinning inks are printed and subsequently cured (Lewis and Gratson 2004). Direct ink writing has been used to print a broad range of materials, including polymers, hydrogels, and polymers reinforced with nanocellulose and other fibers (Barry et al. 2009; Compton and Lewis 2014; Hardin et al. 2015; Gladman et al. 2016; Siqueira et al. 2017; Wang et al. 2018). The printing process can be exploited to align fibers in composites; for example, alignment and improved mechanical properties in specific directions has been shown in 3D printed nanocellulose-polymer composites (Gladman et al. 2016; Siqueira et al. 2017).

There are several reports of additive manufacturing of neat cellulose materials. Nanocellulose structures with complex patterns have been printed from an ionic liquid bacterial nanocellulose suspension (Marksteadt et al. 2014). Neat cellulose nanocrystals (CNCs), which have significantly lower aspect ratios than CNFs, were printed via direct ink writing and alignment of CNCs was demonstrated (Siqueira et al. 2017). Centimeter-scale anisotropic structures of

cellulose acetate have been printed and the resulting materials had a Young's modulus of 2.2 GPa and tensile strength of 45 MPa in specific directions (Pattinson and Hart 2017). Only a few studies have investigated 3D printing of CNFs. Two types of CNFs, TEMPO oxidized CNFs and C-Periodite low aspect ratio fibrils (lengths less than 200 nm), were printed by Rees et al. (2015) into 3D scaffold structures and grid constructs and dried via freeze drying. While 3D scaffold structures and grids could be printed for the low aspect ratio cellulose fibers, structures composed of the TEMPO CNF collapsed (Rees et al.). To the best of our knowledge, only one study has successfully demonstrated printing of neat CNF structures that maintain their geometry (Hakansson et al. 2016). In that work, 3D printed CNF structures were manufactured using air drying with surfactants, solvent exchange, and freeze drying. The tensile properties of materials made by freeze drying and air drying had Young's modulus and tensile strength of 0.031 ± 0.019 GPa/3.9 ± 2.7 MPa and 4.3 ± 0.3 GPa/114 ± 14 MPa, respectively (Hakansson et al. 2016). While progress has been made in printing cellulose materials, the mechanical properties of the printed cellulose materials summarized above are significantly lower than the mechanical properties achieved in thin CNF sheets prepared via the drying techniques discussed in the "Introduction".

There are a variety of routes to prepare CNFs and these determine the fibril size and the affinity between fibrils, which ultimately influence the stiffness and strength of the films comprised of CNFs and partially contribute to the variation of mechanical properties reported in different studies. The thickness of the CNF films manufactured through dish drying, oven drying, or filtration is limited due to large stresses that develop during the drying process. The maximum thicknesses of neat films reported to date is 80 μm for films comprised of microfibrillated cellulose (Henriksson et al. 2008) and 70 μm for films comprised of CNFs (Baez et al. 2014). For low volume fractions of CNFs (< 1 wt%) large residual stresses develop during drying. For higher volume fractions of CNFs, fiber agglomeration and the formation of networks often prevent uniform drying. Thus, control of the water removal process and resulting residual stresses are critical in order to realize bulk neat cellulose materials comprised of CNFs, especially when the thickness exceeds approximately 70 μm.

3D printing is a technique that has the potential to reduce overall drying times and residual stresses because a single printed layer has a high surface area-to-volume ratio and thicker materials can be built up layer-by-layer. To additively manufacture bulk CNF materials, there is a need to first understand the mechanics of individual printed layers and materials comprised of a small number of stacked printed layers. The objectives of this work are to: (1) print CNF thin films with high specific stiffness and strength, comparable with properties obtained in thin films prepared via conventional drying techniques, and (2) to investigate the role of printing conditions on the printed geometry and process performance. Specifically, this paper reports printing of an aqueous cellulose nanofibril suspension and demonstrates repeatable printing of films with high Young's modulus and moderate tensile strength, uniform mechanical properties across the printed specimens, and thicknesses greater than 60 μm.

Methods

Cellulose nanofibrils

CNFs with diameters of approximately 10 nm and aspect ratios > 100 are produced at the USDA Forest Products Laboratory via a modified procedure from Saito et al. that uses TEMPO (2,2,6,6-tetramethylpiperidine-1-oxly-radical) pretreatment (Saito et al. 2007; Reiner and Rudie 2013). The TEMPO pretreatment reduces the required energy, carboxylates the cellulose fibers, and increases water absorption (Pääkkö et al. 2007; Saito et al. 2007). Commercial machine-dried bleached eucalyptus kraft pulp is used as source material and repulped at 8% solids for 1 h. The resulting pulp is then diluted to 2% solids and treated for 12 h at room temperature with 2 wt% $NaClO_2$, pH 2. Following this, the pulp is washed, filtered, and phosphate buffered for 1 h at pH 12 before TEMPO and $NaClO_2$ are added. The pH of the final solution is adjusted to pH 7 using phosphoric acid and NaOH at 60 °C for 3 days. After the pH adjustment the solution is filtered and washed. Then, the solution is diluted, refined, and passed through a homogenizer which breaks apart entangled fibrils and improves optical clarity. The resulting solution is gelatinous with 0.91 wt% CNFs and a charge content

of 1.52 mmol-COONa/g dry CNF. This process has a high yield, with 50% fibrils forming a gel at 0.5–1.0% solids (Qing et al. 2013). The morphology of TEMPO CNFs made via the process used here has been previously characterized by several researchers, e.g. Isogai et al. (2011) and Isogai and Bergstrom (2018). Uniformity of these CNFs is a primary factor in the popularity of the TEMPO process.

3D printing of CNF solutions

CNF aqueous suspensions (0.91 wt%) were printed in various arrangements (Fig. 1) using an extrusion-based process in a custom 3D printer. The printer was constructed by starting with a commercial 3D printer (i3PRO, MakerFront) and replacing the heated extruder head with a syringe connected to an electronically-controlled regulator that modulates the pressure applied to dispense the ink (i.e. CNF suspension) from the syringe. For all experiments, the syringe was fitted with a 30 gauge (150 µm inner diameter) blunt ended needle as the nozzle. The pressure in the syringe was adjusted over a range of 0–413 kPa to control the volumetric flow rate of ink through the nozzle. The printer has a heated bed with a range from room temperature to approximately 100 °C. In most of the experiments, the CNF materials were printed on glass build plates that were solvent cleaned (acetone, methanol, then isopropanol), dried with N_2, plasma treated, and functionalized with trichloro(1*H*,1*H*,2*H*,2*H*-perfluorooctyl) silane using vacuum vapor deposition. This pretreatment made the glass build plate hydrophobic, which influenced the shape of the profiles of the printed lines and facilitated removal of the structures after they are dried. Structures that were characterized via nanoindentation were printed on monocrystalline silicon wafers that were prepared with the same surface treatment as the glass plates. The silicon wafers were used as substrates for films characterized via nanoindentation because they had lower surface roughness and better flatness than the glass build plates.

The volumetric flow rate of the CNF solution through the nozzle, Q_V, as a function of pressure was determined by printing lines of 0.91 wt% CNF suspension onto a glass substrate at room temperature. The lines were deposited over a fixed time interval and the mass of the printed material was measured on a precision balance (Scout Pro, Ohaus) immediately after printing. The velocity of the print head was kept constant at 10 mm/s and the back pressure was varied. The volume dispensed was calculated from the measured mass and the density of the suspension (1004 kg/m^3).

CNF solutions were printed as specimens comprised of a single line/single layer, single line/multiple layers, or multiple lines/multiple layers geometry (Fig. 1) in the current study. Single line/single layer prints, used to assess the cross-sectional geometry of the lines, were printed on glass build plates using print

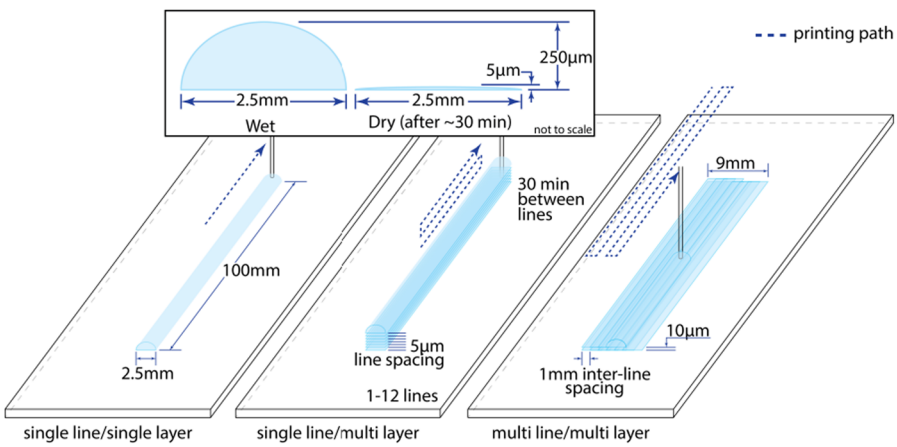

Fig. 1 Schematic of the 3D printing paths. The inner diameter of the blunt ended needle used as the print nozzle was 150 µm. The three types of prints in this work include single line/single layer, single line/multiple layer and multiple line/multiple layer. The printing paths for each type of print is shown in the schematic. The significant change in the height of the line from just printed to dry is shown in the figure inset

head velocities from v = 10 to 45 mm/s and substrate temperatures from 25 to 70 °C. Single line/single layer geometries were printed with a print velocity of 27.5 mm/s and a substrate temperature of 70 °C on silicon wafers for mechanical property characterization via nanoindentation. For all the single line/single layer prints, the back pressure in the syringe was kept constant at 172 kPa and the ambient temperature and relative humidity were 23 °C ± 2 °C and 34% ± 1%, respectively.

To characterize the ability to build thicker structures in a layer-by-layer fashion, single line/multiple layers were printed at a velocity of 27.5 mm/s, substrate temperature of 70 °C, and extrusion pressure of 172 kPa. Subsequent layers were printed after the previous layer dried for 30 min. Specimens composed of a varying number of layers, n, were printed, with n = 1, 2, 3, 4, 5, 6, 8, and 12. Specimens for tensile testing were prepared by printing multiple line/multiple layers consisting of 6 line passes and 2 layers. The line-to-line spacing was 1.5 mm, providing 1.0 mm of overlap between neighboring lines and contributing to an increased height per layer as compared with the single line prints. The substrate temperature, print velocity, extrusion pressure, and elapsed time between layer depositions were the same as for the single line/multiple layer prints described above. The print direction was along the length of the specimen and the overall dimensions of the specimens were approximately 5.5 mm by 100 mm. The actual width of each specimen was measured via bright-field optical microscopy (Axio Imager, Zeiss) and mechanical profilometry (described below). The specimen thickness was measured with a digital micrometer and verified by mechanical profilometry.

Characterization of cross-sectional and surface geometry

A mechanical profilometer (P7, KLA-Tencor) with a stylus of radius 2 μm, applied load of 2 mg, scan speed of 2000 μm/s, and sampling frequency of 500 Hz was used to measure the cross-sectional shape of the printed lines. Each line was scanned in 5 locations along the length of the lines. Atomic force microscopy (AFM) was used to characterize the surface topography of the printed CNF structures. Imaging was performed via a tapping mode imaging in a commercial AFM (Dimension Icon AFM, Bruker) with a sharp-tipped silicon cantilever with tip radius < 10 nm (ARROW-NCR, NanoAndMore). The images were 5 μm by 5 μm with a resolution of 102 lines/μm.

Nanoindentation

Nanoindentation measurements (TI 950 Triboindenter, Hysitron) of single line/single layer prints on silicon substrates were performed to assess variations in reduced modulus across the printed line. Indentation measurements on two specimens printed at a substrate temperature of 70 °C during drying were performed with two indenters: a diamond Berkovich tip and a conospherical tip with a radius 0.814 μm. The temperature and relative humidity during the nanoindentation measurements were 25.7 ± 0.3 °C and 24.6 ± 1.9%RH, respectively. Arrays of nanoindentation measurements were performed to map material homogeneity (Fig. 2). Local grids of nanoindentation tests consisted of three 5 × 5 measurement arrays with the indents spaced 50 μm apart. These grids were set up along the length of the line approximately 1 mm apart, spanning a total length greater than 10 mm. The properties across the width of a printed line were mapped using a 5 × 40 array that spanned 2.0 mm across the width of the line (Fig. 2). The indents were spaced 50 μm apart. Nanoindentation measurements were performed in load control with a maximum load of 200 μN and a loading and unloading rate of 20 μN/s. The peak load was held for 2 s. The reduced modulus was determined from the nanoindentation load–displacement curves by determining the initial stiffness, S, from a fit to the unloading curve and knowledge of the area of indenter, A, from the experimentally measured area function of the tip. The reduced modulus, E_r, of the specimen is calculated as (Oliver and Pharr 1992)

$$E_r = \frac{S\sqrt{\pi}}{2\sqrt{A}}. \quad (1)$$

Note, Eq. (1) assumes the material tested has isotropic mechanical properties, and the reduced modulus is $E/(1 - \nu^2)$, where E is the Young's modulus and ν is the Poisson's ratio.

Tensile testing

Tensile testing was performed in a uniaxial testing machine (Criterion Model 43, MTS) equipped with a

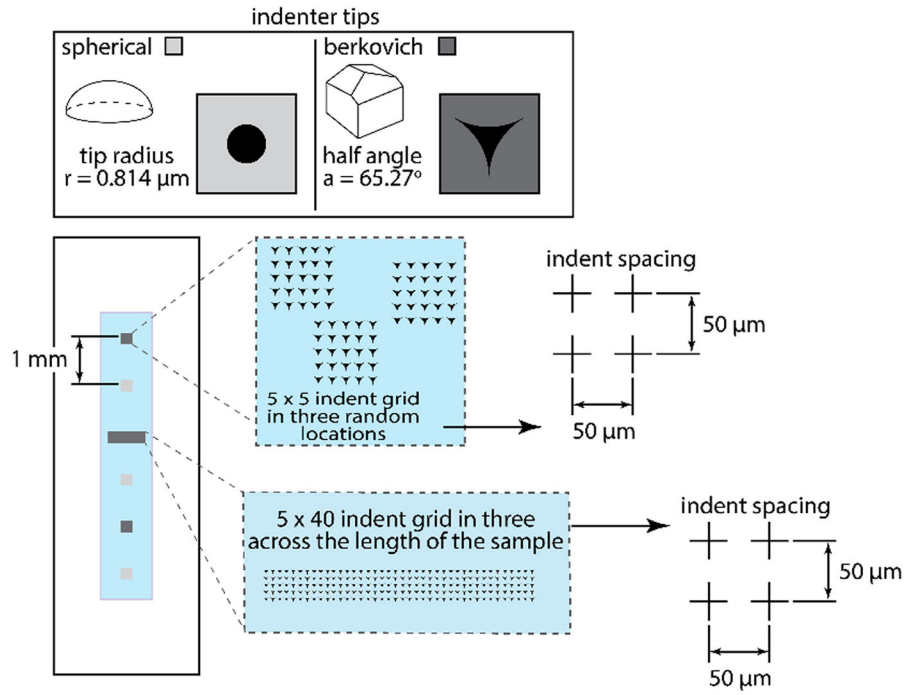

Fig. 2 Schematic of the nanoindentation experiments on a single line/single layer print. The dark grey boxes indicate regions indented by the Berkovich indenter. The light grey boxes indicate regions indented by the spherical tip. The tip geometries are shown in the top box

50 N load cell (LSB.501, MTS). The displacement rate was 1 mm/min. in all tests. A total of 8 specimens were tested. Specimen widths were 5.5 mm ± 0.46 mm and gauge lengths varied from 45 to 54 mm; a gauge length-to-width ratio of greater than 8:1 was maintained for all specimens. The nominal strain rates varied from 0.75 to 0.9 s^{-1}. The bilayer specimens used for tensile testing had a thickness of 32.7 µm ± 3.3 µm. Four specimens were marked with thin metallic flakes (i.e. glitter) on the surface with a diameter of approximately 0.23 mm to track displacements using digital image correlation (DIC). Four specimens were left unmarked and displacements were tracked by following features in the material. Images of the specimens during the test were captured with a digital camera (Guppy Pro F-201B, Allied Vision, resolution of 1624 × 1234 pixels) fitted a manual focus lens (HR F2.8/50 mm, Navitar); the field of view was 29.3 × 21.9 mm. The force, displacement, and image data were collected using a Matlab script that synchronized all data. For each specimen, the measured force, F, and crosshead displacement, d, data were fit with a hyperbolic tangent expression (Suhling 1985):

$$F = b_1 \tanh(b_2(d - b_4)) + b_3(d - b_4), \quad (2)$$

where b_1, b_2, b_3, b_4, are fitting parameters. The Young's modulus, E, was determined by evaluating the stiffness of the specimen (i.e., first derivative of Eq. (2) with respect to d) at $d = 0$ and accounting for the cross-sectional area, A, and the gauge length, L, of the specimen:

$$E = \frac{L}{A}\left(b_1 b_2 sech^2(b_2 b_4) + b_3\right). \quad (3)$$

DIC measurements provided strain measurements at small strains, typically less than about $5(10^{-3})$. To obtain strain measurements up to the failure point, crosshead displacement data was used. For each specimen, the crosshead displacement data was corrected for machine compliance based on the DIC measurements at small strains.

Results and discussion

Characterization of CNF printing

The volumetric flow rate through the print nozzle, Q_v, was measured as a function of back pressure in the syringe (Fig. 3). CNF suspensions are shear thinning

(Compton and Lewis 2014), yet the high shear rate behavior ($> 10^4$ s^{-1}) has not been characterized. The shear rates, corresponding to the flow rates in Fig. 3, ranged from $9.5(10)^4$ to $2.5(10)^5$ s^{-1}. The results in Fig. 3 show that the flow rate of ink can be precisely controlled via modulation of pressure. For all subsequent printing experiments, a back pressure of 172 kPa was used.

The effects of print conditions on the geometry of the printed lines, once dry, were determined from print experiments and subsequent characterization via mechanical profilometry. Mechanical profilometry measurements of the printed single line/single layer geometries (Fig. 4a) show that the line profiles were strongly influenced by substrate temperature. Specifically, a valley developed on the top surface of the lines printed on heated substrates and became more pronounced as the substrate temperature was increased. The shape of material deposited on a substrate resulting from drying a colloidal drop/line is complex and depends on multiple factors, including pinning of the contact line, transport of the solids due to flow within the drops during drying, and gelation of the suspension as the concentration in the evaporating solution increases (Pauchard and Allain 2003; Okuzono et al. 2009). We imaged the drying lines optically from above and observed that the contact line moves as the printed line dries and CNFs are deposited on the substrate, consistent with previous observations of drying drops of CNF solution (Skogberg et al. 2017). As the temperature is increased, the evaporation rate increases, leading to a rapid increase in concentration

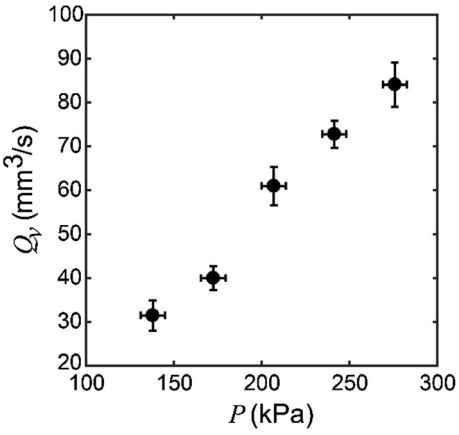

Fig. 3 The volumetric flow rate, Q_v, of the CNF ink through the nozzle as a function of applied pressure, P

of CNFs at the ink/air interface. This high concentration of CNFs can result in a gel-like layer or "skin" near the interface, the formation of which can significantly affect the profile of the dried line (Okuzono et al. 2009). Direct comparisons between the results here and the significant body of work on drying of pinned drops (e.g. the "coffee ring" effect) cannot be made as the contact line here is not pinned, however profiles similar to those in Fig. 4 arise in pinned drops (Pauchard and Allain 2003; Okuzono et al. 2009). We hypothesize that the line profile evolves with temperature as observed because higher temperature leads to faster evaporation, which alters the flow of CNFs within the printed line during drying as well as the time it takes to a form a high CNF concentration skin-like gel layer. Ultimately, the final profile depends on the interplay of these two factors as transport of CNFs within the line affects the distribution of CNFs within the line and redistribution of the CNFs is limited after a gel forms.

The line height and width are determined from profilometry measurements like the examples shown in Fig. 4a. The line width is denoted as the width at the base of the line profile. The line height was determined as the distance from the base to peak of the line profile, or the average value between the peaks for profiles with multiple peaks. Line width as a function of the print velocity is shown in Fig. 4b. Data was collected at four temperatures (25 °C, 37 °C, 50 °C, 70 °C) and no significant dependence of line width on temperature was observed. The line width decreases with increasing print speed and is fit well by a power-law function. The power-law approximation is reasonable as the width is related to the flow rate and print speed through mass conservation.

The material deposition rate, Q, of the dried film is determined using the area of the cross-sections measured via line profilometry. Figure 4c shows the cross-sectional area of the printed lines as a function of the print speed. From mass conservation, the cross-sectional area of the line, A, is expected to be inversely proportional to the print speed, v.

$$A = Qv^{-1} \tag{4}$$

Fitting the above equation to the data in Fig. 4c, the effective dry material deposition rate was $Q = 0.197$ mm^3/s $\pm$ 0.009 mm^3/s.

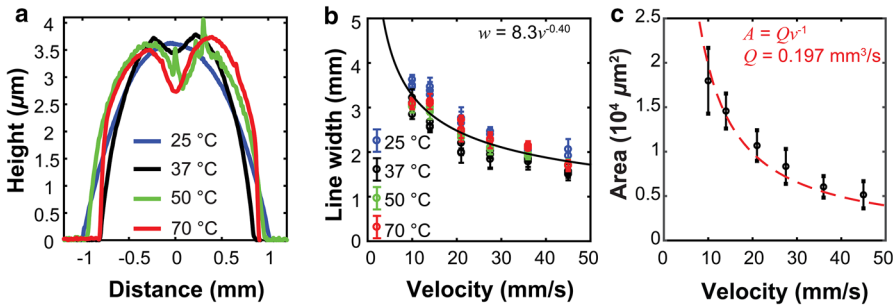

Fig. 4 **a** Representative single line print profiles for v = 45 mm/s and varying substrate temperature, T. **b** Line width, w, of the CNF single line/single layer prints as a function of the print head velocity for specimens printed at 25 °C, 37 °C, 50 °C, and 70 °C. The error bars are the standard deviation of the line width across 3 specimens with 5 measurements per specimen. The data, across all temperatures, is fit with a single power law. **c** Cross sectional area of the CNF single line/single layer prints as a function of the print head velocity for specimens printed at 25 °C, 37 °C, 50 °C, and 70 °C. The error bars represent the standard deviation

The ability to build thicker parts though multilayer printing was first assessed by fabricating single line/multiple layer print geometries (Fig. 1). The specimen thickness as a function of the number of printed layers is shown in Fig. 5a, where each data point represents an average thickness for 3 specimens. A linear fit to the data has a slope of 5.1 μm/layer, which compares well with the thickness of 4.9 μm for $n = 1$. Profiles of the line for different numbers of layers, n, are shown in Fig. 5b. The line width stayed relatively constant (Fig. 5c) with increasing number of layers. Thus, the underlying layers support additional layers and prevent significant volumes of material from flowing over the edges. Due to the high water content of the CNF solution, printing subsequent layers caused the previously printed layers to rehydrate. This rehydration encouraged hydrogen bonds to form between the new layer and the previous layer. Interlaminar strength may be less than intralaminar strength due to differences in fiber entanglement; rehydration was not so complete that fibrils were able to entangle in the z-direction between layers. However, no delamination between layers was observed when the dried multilayer films were removed from the substrate and deformed.

Atomic force microscopy and nanoindentation results

The surface topography of CNF lines printed at 70 °C was characterized using AFM; a representative measurement is shown in Fig. 6a. The r.m.s. roughness measured in the AFM images was 3.63 nm ± 0.21 nm over areas of 10 μm^2; this is based on an average of five measurements on three specimens. Roughness was small compared to the size of the tips used in

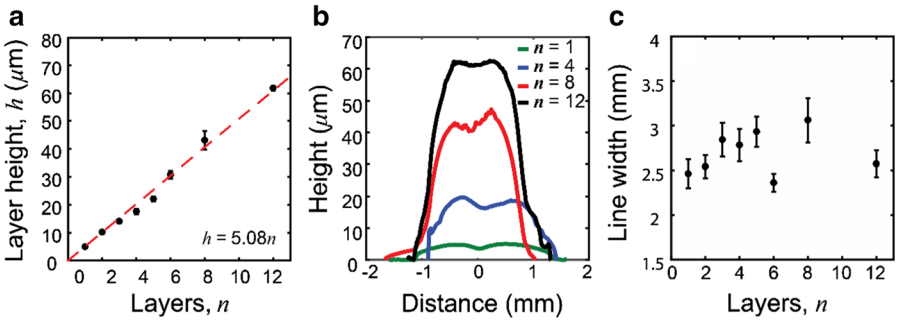

Fig. 5 Geometry of multilayer line prints. **a** Line height of the single line/multiple layer prints as a function of number of layers, n. The error bars represent the standard deviation. A linear fit yields a slope of 5.1 μm/layer. **b** Representative line profile shapes for the single line/multiple layer prints for n = 1,4,8, and 12. **c** Line width of the single line/multiple layer prints as a function of number of layers. The error bars are the standard deviation calculated for multiple specimens

nanoindentation, and thus the fibrous film was treated as a homogenous material for analysis by nanoindentation. The fibers formed a dense film, 84% of the density of native cellulose; this tight packing of the fibers was attributed to high surface tension induced capillary forces during drying (Mashkour et al. 2014; Skogberg et al. 2017).

AFM tapping mode phase images show apparent alignment of the CNFs parallel to the long axis of printed lines (Fig. 6b). A higher magnification AFM image that shows the alignment more clearly is shown in Fig. 6c. Alignment, similar to that shown in Fig. 6c, was observed in AFM images acquired on both printed lines and in tensile specimens and was not dependent on the print path direction (i.e., alignment, like that shown in Fig. 6c, was seen regardless of whether the line was printed in the typical configuration of one pass along the axis of the line or multiple passes across the width of the line). The lack of the dependence on print path, as well as the low CNF concentration and low viscosity of the ink (Kacir et al. 1975), suggests that hydrodynamic alignment from printing through a nozzle is not the dominant factor in inducing alignment. Rather, the alignment is likely induced by the drying process. Skoberg et al. (2017) investigated alignment of CNFs in drying drops and showed alignment of CNFs parallel to the moving contact line and drying front, consistent with the observations here. They hypothesized that the alignment was due to surface-tension induced torque acting on the CNFs at the contact line and capillary forces between fibers once alignment was initially established (Skogberg et al. 2017). It is important to note that AFM images only provide information on alignment in a local region of the line and near the surface, thus more detailed characterization to fully understand alignment is a focus of our ongoing work.

The uniformity of the mechanical properties of printed CNF lines was assessed with nanoindentation, using both a Berkovich and spherical tip. Figure 7a shows a map of the reduced modulus spanning a 250 μm × 250 μm area. Although the observed fiber orientation in Fig. 6 implies the material, and therefore mechanical properties, are likely anisotropic, which violates the isotropic assumption of Eq. (1), the measurements are still valid here for the purpose of assessing the uniformity across and along the length of a single line print. The areas of higher and lower modulus were interspersed with no trend in the variation. The modulus had a small average percent difference of ± 2.3% from the mean of 9.9 GPa and a maximum percent difference of 7.6% from the mean, across the measurement area in Fig. 7a. For the 12 areas that were measured on two different specimens, there was an average percent difference of ± 2.6% and a maximum percent difference of 11.7% from the mean of 9.7 GPa. The arrays of indents were spaced 1 mm apart along a single line/single layer specimen printed at 70 °C spanning a total length of 10 mm. Between the arrays, the indenter was alternated between a Berkovich and spherical tip to assess if the indenter geometry affects the measurements. We measured no significant change in the reduced modulus along the length of the line print and there were minimal differences between the Berkovich and spherical indenters which yielded values of 9.7 ± 0.4 GPa and 9.9 ± 0.4 GPa, respectively. The contact sizes in the measurements performed with the two tip is similar: ≈ 0.33 μm^2 contact area for Berkovich at a nominal contact depth of 100 nm and

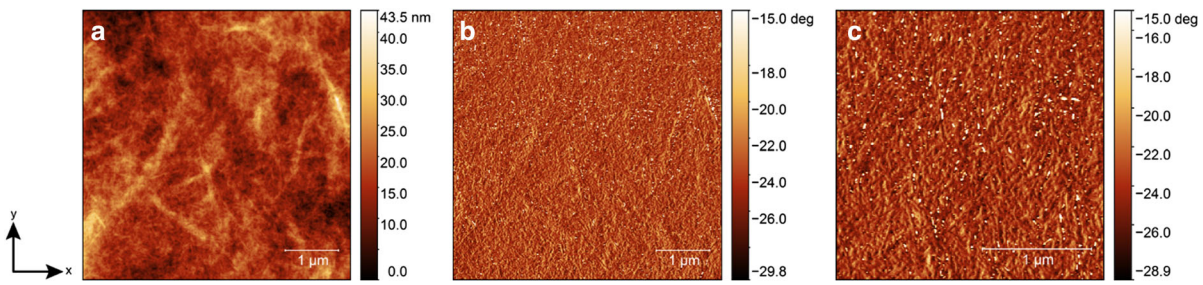

Fig. 6 **a** Tapping-mode AFM topography image of a printed cellulose nanofibril surface. **b** Tapping-mode AFM phase image corresponding to the topography image shown in (**a**). The long axis of the printed line is parallel to the y-axis. **c** Enlarged view of the phase image

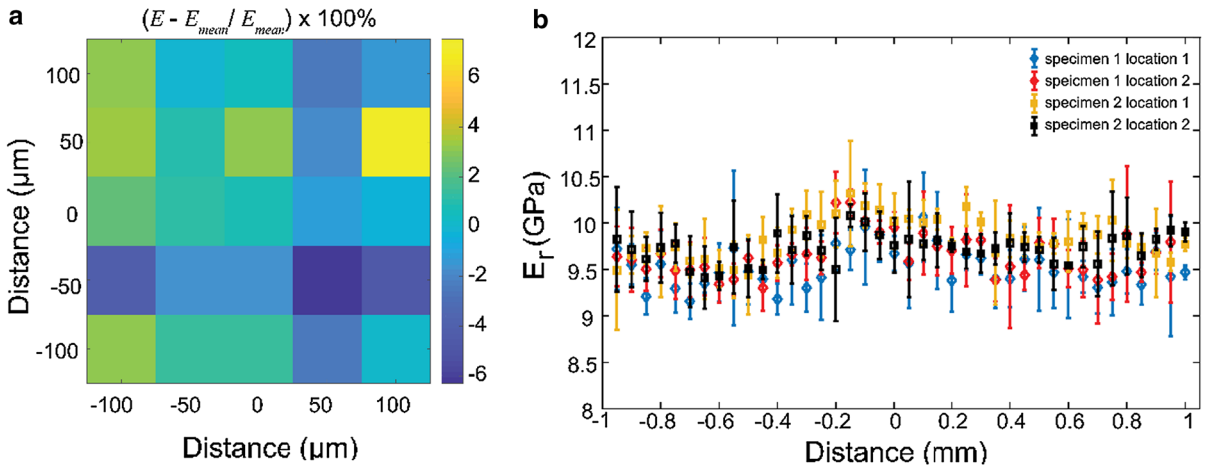

Fig. 7 **a** Percent difference of the reduced modulus as compared with the average reduced modulus in a local grid spanning 250 µm × 250 µm; measurements performed with a Berkovich tip. **b** Reduced modulus across the line width using the Berkovich tip. The data are averaged together over the 5 rows at each point across the line. The error bars are the standard deviation calculated for that average

≈ 0.34 µm^2 contact area for the sphere at a nominal contact depth of 44 nm.

The variation of the reduced modulus across the width of a specimen printed at 70 °C is shown in Fig. 7b. Across the 2 mm section of the line, there was a small variation (< 6.0%) in the reduced modulus in the center region of the print (see Fig. 7b). The relatively uniform reduced modulus suggests a mostly homogeneous material across the printed line, however the increase in modulus near the center suggests the density of the printed material may be slightly higher in the center, which is the same region where a valley is observed in the profilometry measurements (Fig. 4a). Hardness for the CNF specimen dried at 70 °C was also obtained from the nanoindentation and found to be 0.59 GPa ± 0.02 GPa, as measured in tests with the Berkovich indenter. Overall, the uniformity of the mechanical properties along the length and across the width of the printed CNF lines suggests that the material can be treated as globally homogenous in subsequent tensile testing.

Tensile testing

Representative stress strain curves for the bi-layer tension specimens are shown in Fig. 8a. Both crosshead and digital image correlation displacements were used to determine the tensile strains of the CNF strip specimens. The difference between the crosshead and DIC data is expected because of the large axial stiffness of the CNF thin films, which amplifies the effect of compliance within the system when determining strain from crosshead displacement. Additionally, Fig. 8a shows a comparison between the raw crosshead data and the crosshead data corrected for test machine compliance; this demonstrates that crosshead displacements, once corrected for machine compliance, agree with DIC over the full stress–strain curve. Young's modulus determined from DIC is E = 10.2 GPa ± 1.2 GPa. These bilayer 3D printed films have a Young's modulus more than 2× greater than previous reports of 3D printed CNF materials in the literature (Hakansson et al. 2016). Four of the tensile specimens failed in the necked region of the film (as opposed to breaking near the grips) and the stress–strain curves for these specimens are shown in Fig. 8b. The mean tensile strength for these four specimens is 72.6 MPa ± 7.4 MPa.

The density of the CNF tensile specimens was measured to be 1267 ± 131 kg/m^3. This density gives a specific stiffness and specific strength of 8048 ± 1384 kN-m/kg and 57.3 ± 8.3 kN-m/kg, respectively. Careful examination of the printed materials showed occasional edge cracks and voids caused by bubbles in the solution during printing, resulting in a density that is lower than that of pure cellulose (1500 kg/m^3). These defects also likely limited the tensile strength of these materials. Thus, the tensile strength determined here is believed to be a

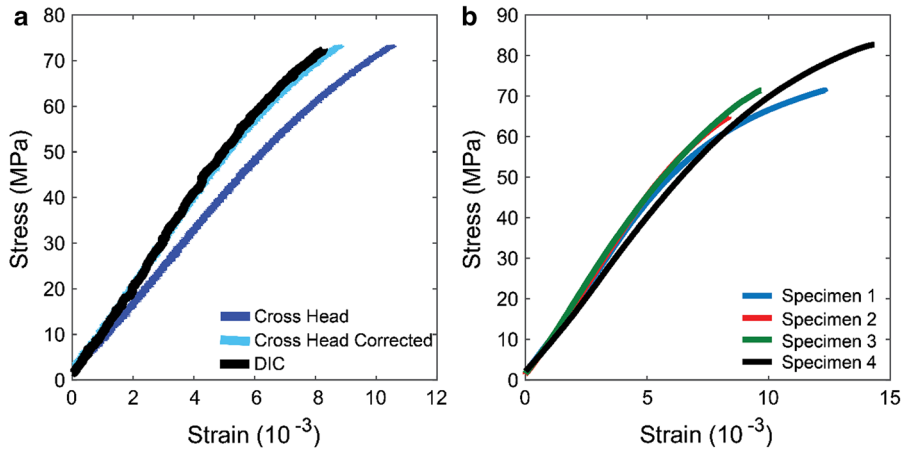

Fig. 8 **a** Stress–strain curves for a representative tensile specimen highlighting the deviation in slope between strain computed from crosshead displacement (dark blue curve) and strain from digital image correlation displacements (black curve). The crosshead displacement data can be corrected for the machine compliance (light blue curve). **b** Stress–strain curves from crosshead displacement corrected for the machine compliance for specimens that failed in the gauge section. (Color figure online)

lower estimate of the potential strength of these 3D printed neat CNF films.

Conclusion

We have developed a system to print CNF suspensions in a controlled and repeatable process. This ability has been demonstrated through evaluation of single line prints as well as printing of multilayer structures. Through the manipulation of drying rates via substrate temperature, we showed that the shape of the dried line profile can be controlled to be flat at the top or have a valley of varying sizes, dependent on substrate temperature. This method of shape control can be exploited to manage how subsequent layers fill in and bond to previously printed layers. Mapping of the mechanical properties revealed that the complex shape of the line profile at elevated substrate temperatures did not show an effect on the reduced modulus, further demonstrating the ability to both control the profile shape and to achieve line prints with uniform mechanical properties. Films with thicknesses greater than 60 μm have been fabricated via multilayer line printing. These thicknesses were achieved within 6 h, a substantially shorter time than would be needed to produce comparable thickness films via dish drying, thus showing the potential to build larger films and ultimately structures via printing. To the best of our knowledge, this is the first study that has additively printed neat CNF suspensions and achieved films with Young's modulus > 10 GPa, comparable to those reported in dish drying techniques. Future work will be aimed at developing a more efficient drying process, examination of fibril alignment, and the effects of fibril alignment on anisotropic mechanical properties.

Acknowledgments This work was supported by the U.S. Endowment for Forestry and Communities, Inc. as part of the P^{3}Nano program. This work was performed in part at the University of Pennsylvania's Singh Center for Nanotechnology, an NNCI member supported by NSF Grant ECCS-1542153. The authors thank Dr. Joseph E. Jakes (USDA Forest Service, Forest Products Laboratory) for insightful nanoindentation discussions. The authors also thank Dr. Alexander I. Bennett (University of Pennsylvania) for helpful discussions and assistance in preparing Figs. 1 and 2.

References

Aulin C, Salazar-Alvarez G, Lindström T (2012) High strength, flexible and transparent nanofibrillated cellulose–nanoclay biohybrid films with tunable oxygen and water vapor permeability. Nanoscale 4:6622. https://doi.org/10.1039/c2nr31726e

Baez C, Considine J, Rowlands R (2014) Influence of drying restraint on physical and mechanical properties of nanofibrillated cellulose films. Cellulose 21:347–356. https://doi.org/10.1007/s10570-013-0159-1

Barry RA, Shepherd RF, Hanson JN et al (2009) Direct-write assembly of 3D hydrogel scaffolds for guided cell growth.

Adv Mater 21:2407–2410. https://doi.org/10.1002/adma.200803702
Berman B (2012) 3-D printing: the new industrial revolution. Bus Horiz 55:155–162. https://doi.org/10.1016/j.bushor.2011.11.003
Carpenter AW, de Lannoy C-F, Wiesner MR (2015) Cellulose nanomaterials in water treatment technologies. Environ Sci Technol 49:5277–5287. https://doi.org/10.1021/es506351r
Compton BG, Lewis JA (2014) 3D-printing of lightweight cellular composites. Adv Mater 26:5930–5935. https://doi.org/10.1002/adma.201401804
Fukuzumi H, Saito T, Iwata T et al (2009) Transparent and high gas barrier films of cellulose nanofibers prepared by TEMPO-mediated oxidation transparent and high gas barrier films of cellulose nanofibers prepared by TEMPO-mediated oxidation. Biomacromol 10:162–165. https://doi.org/10.1021/bm801065u
Gladman AS, Matsumoto EA, Nuzzo RG et al (2016) Biomimetic 4D printing. Nat Mater 15:413–418. https://doi.org/10.1038/nmat4544
Gross BC, Erkal JL, Lockwood SY et al (2014) Evaluation of 3D printing and its potential impact on biotechnology and the chemical sciences. Anal Chem 86:3240–3253. https://doi.org/10.1021/ac403397r
Hakansson KMO, Henriksson IC, de la Peña Vazquez C et al (2016) Solidification of 3D printed nanofibril hydrogels into functional 3D cellulose structures. Adv Mater Technol. https://doi.org/10.1080/01425690701737481
Hardin JO, Ober TJ, Valentine AD, Lewis JA (2015) Microfluidic printheads for multimaterial 3D printing of viscoelastic inks. Adv Mater 27:3279–3284. https://doi.org/10.1002/adma.201500222
Henriksson M, Berglund LA, Isaksson P et al (2008) Cellulose nanopaper structures of high toughness. Biomacromol 9:1579–1585. https://doi.org/10.1021/bm800038n
Isogai A (2013) Wood nanocelluloses: fundamentals and applications as new bio-based nanomaterials. J Wood Sci 59:449–459. https://doi.org/10.1007/s10086-013-1365-z
Isogai A, Bergstrom L (2018) Preparation of cellulose nanofibers using green and sustainable chemistry. Curr Opin Green Sustain Chem 12:15–21
Isogai A, Saito T, Fukuzumi H (2011) TEMPO-oxidized cellulose nanofibers. Nanoscale 3:71–85. https://doi.org/10.1039/c0nr00583e
Kacir L, Narkis M, Ishai O (1975) Oriented short glass-fiber composites. II. Analysis of parameters controlling the fiber/glycerine orientation process. Polym Eng Sci 15:532–537. https://doi.org/10.1002/pen.760150709
Lewis JA, Gratson GM (2004) Direct writing in three dimensions. Mater Today 7:32–39. https://doi.org/10.1016/S1369-7021(04)00344-X
Malho JM, Laaksonen P, Walther A et al (2012) Facile method for stiff, tough, and strong nanocomposites by direct exfoliation of multilayered graphene into native nanocellulose matrix. Biomacromol 13:1093–1099. https://doi.org/10.1021/bm2018189
Marksteadt K, Sundberg J, Gatenholm P (2014) 3D bioprinting of cellulose structures from an ionic liquid. 3D Print Addit Manuf. https://doi.org/10.1080/01425690701737481
Mashkour M, Kimura T, Kimura F et al (2014) Tunable self-assembly of cellulose nanowhiskers and polyvinyl alcohol chains induced by surface tension torque. Biomacromol 15:60–65. https://doi.org/10.1021/bm401287s
Okuzono T, Kobayashi M, Doi M (2009) Final shape of a drying thin film. Phys Rev E Stat Nonlinear Soft Matter Phys 80:1–11. https://doi.org/10.1103/PhysRevE.80.021603
Oliver WC, Pharr GM (1992) An improved technique for determining hardness and elastic modulus using load and displacement sensing indentation experiments. J Mater Res 7:1564–1583. https://doi.org/10.1557/JMR.1992.1564
Pääkkö M, Ankerfors M, Kosonen H et al (2007) Enzymatic hydrolysis combined with mechanical shearing and high-pressure homogenization for nanoscale cellulose fibrils and strong gels. Biomacromol 8:1934–1941. https://doi.org/10.1021/bm061215p
Pattinson SW, Hart AJ (2017) Additive manufacturing of cellulosic materials with robust mechanics and antimicrobial functionality. Adv Mater Technol 2:1600084. https://doi.org/10.1002/admt.201600084
Pauchard L, Allain C (2003) Buckling instability induced by polymer solution drying. Euorphysics Lett 62:897–903. https://doi.org/10.1209/epl/i2005-10093-3
Qing Y, Sabo R, Zhu JY et al (2013) A comparative study of cellulose nanofibrils disintegrated via multiple processing approaches. Carbohydr Polym 97:226–234. https://doi.org/10.1016/j.carbpol.2013.04.086
Rees A, Powell LC, Chinga-Carrasco G et al (2015) 3D bioprinting of carboxymethylated-periodate oxidized nanocellulose constructs for wound dressing applications. Biomed Res Int. https://doi.org/10.1155/2015/925757
Reiner RS, Rudie AW (2013) Pilot plant scale-up of TEMPO pretreated cellulose nanofibrils. In: Postek M, Moon RJ, Rudie AW, Bilodeau MA (eds) Production and applications of cellulose nanomaterials. TAPPI Press, Peachtree Corners, pp 177–178
Saito T, Kimura S, Nishiyama Y, Isogai A (2007) Cellulose nanofibers prepared by TEMPO-mediated oxidation of native cellulose. Biomacromol 8:2485–2491. https://doi.org/10.1021/bm0703970
Sehaqui H, Ezekiel Mushi N, Morimune S et al (2012) Cellulose nanofiber orientation in nanopaper and nanocomposites by cold drawing. ACS Appl Mater Interfaces 4:1043–1049. https://doi.org/10.1021/am2016766
Shatkin JA, Wegner TH, Bilek EM, Cowie J (2014) Market projections of cellulose nanomaterial-enabled products—Part 1: applications. Nanocellulose Mark 13:9–16
Siqueira G, Kokkinis D, Libanori R et al (2017) Cellulose nanocrystal inks for 3D printing of textured cellular architectures. Adv Funct Mater 27:1604619. https://doi.org/10.1002/adfm.201604619
Skogberg A, Mäki AJ, Mettänen M et al (2017) Cellulose nanofiber alignment using evaporation-induced droplet-casting, and cell alignment on aligned nanocellulose surfaces. Biomacromol 18:3936–3953. https://doi.org/10.1021/acs.biomac.7b00963
Suhling JC (1985) Constitutive relations and failure predictions for nonlinear orthotropic media, vol 1. University of Wisconsin-Madison, Madison
Wang Q, Sun J, Yao Q et al (2018) 3D printing with cellulose materials. Cellulose. https://doi.org/10.1007/s10570-018-1888-y

Wu CN, Saito T, Fujisawa S et al (2012) Ultrastrong and high gas-barrier nanocellulose/clay-layered composites. Biomacromol 13:1927–1932. https://doi.org/10.1021/bm300465d

Zhu H, Zhu S, Jia Z et al (2015) Anomalous scaling law of strength and toughness of cellulose nanopaper. Proc Natl Acad Sci 112:8971–8976. https://doi.org/10.1073/pnas.1502870112